Radial Anisotropy and Prior Petrological Constraints: a Comparative Study

C. Beghein

Earth and Space Sciences Department, UCLA, Los Angeles, CA

C. Beghein, Earth and Space Sciences Department, University of California Los Angeles, 595 Charles Young Drive East, Box 951567, Los Angeles, CA 90095-1567 (cbeghein@ess.ucla.edu)

Abstract.

Radial seismic anisotropy models are traditionally obtained using empirical constraints based on laboratory experiments and petrological considerations. We tested the hypothesis that such petrological constraints affect the uppermost mantle models of S-wave anisotropy using a statistical approach. In addition, we were able to determine which model features are constrained by the data and which are dominated by the prior. We focused on large-scale models, and found that the most likely models obtained in both cases are highly correlated. This demonstrates that for the best data-fitting solution, the geometry of uppermost mantle radial anisotropy is not strongly affected by prior petrological constraints. The amplitude of the anomalies, however, can change significantly : The best data-fitting model obtained without petrological constraints displays stronger amplitudes than the one obtained with prior. This could become an issue when quantitatively interpreting seismic anisotropy models, and thus emphasizes the importance of accurately accounting for parameter uncertainties and trade-offs, and of understanding whether the seismic data or the prior constraints the model. We showed that model uncertainties are strongly affected by the prior as the relative rms uncertainties were reduced by a factor two. In addition, we showed that while the model distributions are not necessarily Gaussian *a priori*, imposing petrological constraints can force the distributions to be narrower and more Gaussian-like, as expected from inverse theory. Finally, we demonstrated that the age-dependence of seismic wave velocities is robust and independent of prior constraints. A

similar age signal exists for anisotropy, but with larger uncertainties without prior constraints.

1. Introduction

Accurately modeling mantle seismic anisotropy, that is the dependence of seismic wave velocity with the direction of propagation or polarization, can help us understand mantle deformation [*Karato and Toriumi*, 1989; *Kendall et al.*, 2000; *Becker et al.*, 2003], the coupling between lithosphere and asthenosphere [*Silver and Holt*, 2002; *Becker et al.*, 2006b], mantle composition [*Montagner and Anderson*, 1989], rheology [*Becker et al.*, 2008], and the net rotation of the lithosphere [*Becker*, 2008]. However, despite numerous efforts to model mantle seismic anisotropy over the past 20 years, uncertainties remain on its exact depth extent and lateral variations in the uppermost mantle, on its presence in the transition zone, and on its global nature in the D" layer [*Fouch and Fischer*, 1996; *Montagner and Kennett*, 1996; *Ekström and Dziewonski*, 1998; *Lay et al.*, 1998; *Trampert and van Heijst*, 2002; *Wookey et al.*, 2002; *Gung et al.*, 2003; *Panning and Romanowicz*, 2006; *Beghein and Trampert*, 2004a, b; *Beghein et al.*, 2006; *Panning and Romanowicz*, 2006; *Zhou et al.*, 2006; *Marone et al.*, 2007; *Nettles and Dziewonski*, 2008; *Beghein et al.*, 2008].

Discrepancies between models can arise for a variety of reasons. To fully describe Earth's elastic properties one would ideally want to determine the 21 independent elements of the fourth-order elastic stiffness tensor, at a given time and location inside Earth. In practice, this is challenging because seismic data are only sensitive to subsets of those 21 elements [*Tanimoto*, 1986; *Chen and Tromp*, 2007; *Beghein et al.*, 2008], and different types of data depend on different subsets of elastic coefficients (see summary tables in *Chen and Tromp* [2007] and *Beghein et al.* [2008]). In addition, while some data, such as shear-wave splitting measurements, can provide precise constraints on lateral changes in seismic anisotropy, their depth resolution is very poor. Surface wave and free oscillation data are better suited to constrain depth changes in structure, but their lateral resolution is lower than that of body waves. This can yield apparent discrepancies and make model comparisons difficult. Moreover, three-dimensional models of seismic anisotropy are typically obtained by data inversion, which is often an ill-posed and ill-conditioned problem. This means that tomographic models are non-unique, i.e. several models can fit the same data equivalently well due to the existence of parameter trade-offs, inherent uncertainties in the data that lead to uncertainties in the models, and the existence of the model null-space, which is the part of the model space that the data cannot constrain.

One way of reducing the parameter trade-offs, and therefore the number of possible solutions, is by jointly inverting data sets that are sensitive to different but overlapping subsets of elastic coefficients. However, this alone is usually not sufficient to uniquely characterize the anisotropic properties of Earth's interior. One can always transform an ill-posed into a well-posed problem by introducing sufficient *a priori* information, and then solving the equations with a regularized least-squares inversion [*Jackson*, 1979; *Jackson and Matsu'ura*, 1985]. The regularization constitutes some kind of *a priori* information. It gives a way of reducing the ensemble of possible solutions, and choosing a particular solution among all the models compatible with the data. However, this also introduces hidden problems that make the resolution assessment of tomographic models less straight-forward than often assumed [*Trampert*, 1998], and the resulting model could be influenced (possibly dominated) by such prior information. In addition, because the regularization imposed is not always based on physical information, our ability of making reliable interpretation of the models can be challenged.

Many levels of regularization are implicitly and explicitly introduced when solving an inverse problem. The physical variables used to describe the Earth are generally expanded onto a set of basis functions, which has to be truncated for practical reasons. This truncation consists in some level of (implicit) regularization and implies that the choice of the basis functions can influence the final model. The choice of the model parametrization (e.g. perturbations in seismic velocities or in elastic parameters, layered depth parametrization or spline functions, etc) is also a form of regularization and can influence the solution as well [*Lévêque and Cara*, 1985]. In addition, a cost function (χ^2 misfit, variance reduction, etc) is typically minimized, and the choice of this cost function consists in an explicit form of regularization. It involves an arbitrary choice of model space norm $\Delta_{\mathcal{M}}$ to measure the distance between the solution $\mathbf{m}$ and a reference model $\mathbf{m}_0$ (which itself is chosen *a priori*), and a choice of data space norm $\Delta_{\mathcal{D}}$ for the distance between observations $\mathbf{d}$ and predictions $\mathbf{Am}$ (in the case of a linear problem). A general form of the cost function is [*Tarantola*, 1987] :

$$C_\lambda = \Delta_{\mathcal{D}}(\mathbf{d}, \mathbf{Am}) + \lambda \Delta_{\mathcal{M}}(\mathbf{m}, \mathbf{m}_0). \quad (1)$$

λ is called the trade-off parameter. Its value is chosen arbitrarily when minimizing the cost function, and it compromises between optimizing the data fit and some information in the model space (norm, gradient, second derivatives, etc). The data space norm is typically chosen as: $\Delta_{\mathcal{D}}(\mathbf{d}, \mathbf{Am}) = (\mathbf{d} - \mathbf{Am})^\dagger \mathbf{C}_d^{-1}(\mathbf{d} - \mathbf{Am})$, where $\mathbf{C}_d$ is a data covariance matrix and † stands for the transpose of a matrix. The data covariance matrix is often reduced to a diagonal matrix containing estimates of data uncertainties. An example of model space norm is $\Delta_{\mathcal{M}}(\mathbf{m}, \mathbf{m}_0) = (\mathbf{m} - \mathbf{m}_0)^{\dagger}\mathbf{C}_{\mathbf{m}}^{-1}(\mathbf{m} - \mathbf{m}_0)$, where the model covariance matrix $\mathbf{C}_m$ should ideally be chosen using independent prior information on the model space [*Tarantola*, 1987].

Radial anisotropy is a particular case of seismic anisotropy, which occurs when the medium can be characterized by one symmetry axis pointing in the radial direction, and which can be modeled with surface waves or normal mode data. In the case of inversions of these data, prior information on the model space is often introduced in order to reduce the number of unknowns. This can also significantly decrease computing times. The problem is solved only for the best resolved parameters, i.e. shear-wave anisotropy ξ and shear-wave velocity anomalies dV_s, while other parameters are forced to behave according to empirical scaling relationships [*Nishimura and Forsyth*, 1989; *Montagner and Anderson*, 1989; *Gung et al.*, 2003; *Panning and Romanowicz*, 2004, 2006; *Marone et al.*, 2007], or are simply neglected [*Maggi et al.*, 2006; *Marone and Romanowicz*, 2007b]). Using results from laboratory experiments, extrapolated down to a depth of 400km, *Montagner and Anderson* [1989] determined that the parameters describing radial anisotropy correlate with one another, and they calculated empirical scaling relationships based on their results. These prior scaling relationships are often used in inversions of surface wave measurements to constrain radial anisotropy : density anomalies and the three elastic parameters describing P-wave propagation in a transversely isotropic medium (A, C, and F in the notation of *Love* [1927]) are kept proportional to the two shear-wave related elastic parameters (N and L [*Love*, 1927]). These correlations between anisotropic parameters appear to be consistent with deformation-induced lattice preferred orientation (LPO) of minerals [*Becker et al.*, 2006a]. However, the same proportionality factors are generally used at all latitudes and longitudes, at a given depth, and the validity of this approach, as opposed to using laterally variable values, is not clear [*Beghein and Trampert*, 2004a; *Beghein et al.*, 2006].

Several authors reported that the values chosen for the proportionality factors between anisotropic parameters do not affect the main features of the models obtained (e.g. *Nishimura and Forsyth* [1989] for the Pacific Ocean, and *Gung et al.* [2003] at the global scale). In addition, *Nishimura and Forsyth* [1989] reported identical results for anisotropy in the Pacific whether prior constraints were used on the parameters or not. However, the models obtained from seismic inversions can be influenced by several sources of regularization, as explained above. It is therefore difficult to assess to what extent the stability of their results is due to the *a priori* information introduced via the regularization or to a low sensitivity of shear-wave anisotropy models to the prior information introduced. Interestingly, *Panning and Romanowicz* [2004] reported a drop in the correlation between shear-wave anisotropy models obtained with and without scaling factors, at depths lower than 100 km and between 600 and 700 km. This could indicate that such global scaling relationships are not valid at those depths, and that they affect the resulting models.

In order to determine the influence of prior petrological constraints on models of shear wave anisotropy and velocity, we need to employ a method that does not introduce explicit regularization on the model parameters (i.e. $\lambda = 0$ and no $\Delta_{\mathcal{M}}$ used) for a given parameterization. This can be done with a direct search approach, or forward modeling, such as the Neighbourhood Algorithm (NA) [*Sambridge*, 1999a, b]. The NA is an efficient model space search technique, which was successfully applied to several global tomography problems [*Resovsky and Trampert*, 2002; *Beghein et al.*, 2002; *Beghein and Trampert*, 2003; *Resovsky and Trampert*, 2003; *Beghein and Trampert*, 2004a, b; *Resovsky et al.*, 2005; *Beghein et al.*, 2006, 2008]. With this algorithm, all the models compatible with a given data set are found, including the model null-space, and robust probabilistic information on the model parameters (posterior probability density functions and trade-offs) are obtained. *Beghein and Trampert* [2004a] had already applied the NA to fundamental mode Love and Rayleigh phase velocity maps to find models of upper mantle anisotropy. In order to get independent probability density functions (or likelihoods) for the different anisotropic parameters, they had not assumed any prior relationship between the variables and did not neglect the parameters to which the data are the least sensitive. Their shear-wave anisotropy models were generally consistent with previous models, but their results questioned the validity of using global prior constraints based on petrological results.

The primary purpose of this manuscript is to isolate and to quantitatively determine the influence of prior petrological constraints on large-scale global models of shear wave radial anisotropy and velocity in the uppermost mantle. Improvements of the current research with respect to previous work [*Nishimura and Forsyth*, 1989; *Gung et al.*, 2003] is that we separate the effects of petrological constraints from the effects of explicit regularization by using a forward modeling approach and comparing models obtained with and without prior petrological constraints. It is clear that models of anisotropy can change with the choice of the phase velocity map used to determine the anisotropy at depth, of the depth parameterizations and possibly of the model space boundaries. However, for the purpose of this paper and to isolate these effects from other types of regularization, we focus on the effect of prior constraints for a given depth parameterization and assuming we know the phase velocity and its uncertainty up to spherical harmonic degree 8. We generated new models of uppermost mantle anisotropy with the NA and using prior petrological constraints, and quantitatively compared the distributions of models obtained with those of *Beghein and Trampert* [2004a] (hereafter referred to as BT04), which were obtained with the same method and data but without prior petrological constraints. In particular, we examine (1) whether imposing prior petrological constraints influences the models of shear wave anisotropy and velocity, and (2) whether the proportionality values used between anisotropic parameters affect the models. In addition to isolating the effect of prior petrological constraints from the effect of explicit regularization, we obtain model distributions instead of one model chosen among all possible solutions with a subjective regularization. These model distributions enable us to make uncertainty estimates on the models, and thus to get robust, quantitative assessments of the reliability of the model features.

2. Data and Parametrization

To make a fair comparison with the BT04 models, we employ the same data set, data uncertainty estimates, measure of misfit, and parametrization in terms of layers and elastic coefficients.

2.1. Data

One can determine shear wave velocity and anisotropy models at depth either from the direct inversion of long-period seismic waveforms [*Woodhouse and Dziewonski*, 1984; *Gung et al.*, 2003], or in a two-step procedure where phase velocity maps are first obtained from the inversion of long-period seismic spectra and those maps are then inverted at depth in order to find three-dimensional velocity and anisotropy models [*Montagner*, 1986]. Here, we adopted the same method as in *Beghein and Trampert* [2004a] and we focused on the second step of the two-step procedure. The data used are global phase velocity maps obtained by *Trampert and Woodhouse* [2003] for fundamental mode Rayleigh and Love waves, from which we determine three-dimensional variations in seismic anisotropy and velocity. It is clear that the construction of phase velocity maps from the raw phase velocity measurements (step 1 of the two-step procedure) involves the introduction of various regularization schemes, which can influence the resulting phase velocity model and thus the models of anisotropy at depth. We want to stress, however, that our goal is not to examine the effect of regularization schemes on the construction of phase velocity maps or on the anisotropy at depth, which is a subject covered by other authors [*Boschi and Dziewonski*, 1999; *Carannante and Boschi*, 2005]. Instead, we want to examine the effect of prior petrological constraints on the models of anisotropy obtained at step 2 (by solving equation 5), assuming we know the phase velocity (i.e., that step 1 is solved).

The phase velocity data used here are the isotropic part of azimuthally anisotropic fundamental mode Rayleigh and Love wave phase velocity maps obtained by *Trampert and Woodhouse* [2003] at periods of 40, 50, 60, 70, 80, 90, 100, 115, 130 and 150 seconds. The reader is referred to the original paper for details about the construction of those maps, the type of regularization employed, the trade-off curves and resolution tests. The maps were initially expanded in terms of spherical harmonics (SH) up to degree 40. Local perturbations $\frac{\delta c}{c}(\theta,\varphi)$ in phase velocity, with respect to the predictions of a spherically symmetric reference model, represent the depth average of perturbations in Earth structure (e.g. *Dahlen and Tromp* [1998]) :

$$_k\left(\frac{\delta c}{c}\right)(\theta,\varphi) = \int_0^a \delta\mathbf{m}(r,\theta,\varphi)\,{}_k\mathbf{K}(r)\,dr \tag{2}$$

where a is the radius of the Earth, θ is the colatitude and φ the azimuthal angle (or longitude) of a point at the surface of the Earth, and ${}_k\mathbf{K}(r)$ is the partial derivative for model parameter $\mathbf{m}(r)$, also called sensitivity kernel. k discriminates between different surface wave periods. Both the phase velocity maps and the perturbations of the model parameters can be expanded on a SH basis [*Edmonds*, 1960]:

$$ {}_k\left(\frac{\delta c}{c}\right)(\theta,\varphi) = \sum_{s=0}^{s_{max}} \sum_{t=-s}^{s} {}_k\left(\frac{\delta c}{c}\right)_s^t Y_s^t(\theta,\varphi) \tag{3} $$

$$ \delta\mathbf{m}(r,\theta,\varphi) = \sum_{s=0}^{s_{max}} \sum_{t=-s}^{s} \delta\mathbf{m}_s^t(r)\, Y_s^t(\theta,\varphi) \tag{4} $$

s is the degree of the spherical harmonic, t is the order, and s_{max} is the degree at which the SH expansions are truncated. In our case, the phase velocity maps of *Trampert and Woodhouse* [2003] were truncated at degree 40. Equation 2 now becomes :

$$ {}_k\left(\frac{\delta c}{c}\right)_s^t = \int_0^a \delta\mathbf{m}_s^t(r)\,{}_k\mathbf{K}(r)\,dr \tag{5} $$

The problem thus naturally separates into individual SH components and we can solve equation 5 for each SH coefficient separately. Like in the BT04 study, we only used SH degrees up to 8, even though the maps are provided up to degree 40. The lower SH degrees are generally not strongly affected by the regularization imposed (a derivative damping in the case of *Trampert and Woodhouse* [2003]) to create the phase velocity maps from path-averaged measurements. From that point of view, the lower degrees can be considered unbiased.

Fundamental mode surface wave phase velocity maps are sensitive to crustal structure and this has to be accounted for before inverting the data. Three-dimensional crustal structure can have strong non-linear effects on the phase velocity measurements and care has to be taken when correcting surface wave data with a crustal model [*Boschi and Ek-*

ström, 2002; *Marone and Romanowicz*, 2007a; *Kustowski et al.*, 2007; *Bozdag and Trampert*, 2008]. Here, we applied the same non-linear crustal corrections as those calculated by *Beghein and Trampert* [2004a] using the crustal model CRUST5.1 of *Mooney et al.* [1998]. The idea behind those non-linear corrections is that the one-dimensional (1-D) reference model (PREM here) is modified locally by replacing structure above the PREM Moho with a more realistic crust. For every new local 1-D model obtained this way, phase velocity predictions are calculated. The difference with the predictions of the initial reference model gives the non-linear contributions of the three-dimensional crustal model to the phase velocity. Note that a crustal model containing seismic anisotropy would be preferable to isotropic model CRUST5.1, but no such global model exists yet. Besides, it is not clear whether a strong seismic anisotropy signal would be present in the crust at the scale we are interested in (SH degrees 0 to 8) since crustal structure tends to rapidly vary laterally.

To determine the data fit of a model, we use the same χ^2 misfit as in BT04 :

$$\chi^2 = \frac{1}{N}\sum_{i=1}^{N}\left[\frac{\delta d_i - (\mathbf{A}\delta\mathbf{m})_i}{\sigma_i}\right]^2 \tag{6}$$

It measures the distance between observations $\delta\mathbf{d}$ and data predictions $\mathbf{A}\delta\mathbf{m}$ in the data space, i.e. the average data misfit compared to the size of the data error bar σ_i. N is the total number of data.

Although the lower SH degrees can be regarded as unbiased with respect to the regularization chosen to produce the phase velocity maps, discrepancies exist between global phase velocity maps obtained by different groups. For instance, *Ekström et al.* [1997] noted strong disagreements in regions of very thick crust (e.g. India and central Asia) between their own phase velocity maps and those produced by *Trampert and Woodhouse*

[1996], especially for Love waves at short periods (40s and below). They showed that the correlation between the 40s Love wave phase velocity maps deteriorate for SH degrees 7 and higher. *Carannante and Boschi* [2005] verified that these discrepancies do not arise from the inversion schemes or the chosen regularizations, and concluded that they originate from the data themselves. It is thus important to estimate uncertainties on the phase velocities. For consistency, we employ the uncertainties determined in BT04, which were based on the standard deviation calculated with phase velocity maps from different studies at periods of 40, 60, 80, 100 and 150 seconds [*Trampert and Woodhouse*, 1995, 1996, 2001, 2003; *Laske and Masters*, 1996; *Ekström et al.*, 1997; *Wong*, 1989; *van Heijst and Woodhouse*, 1999]. At intermediate periods (50, 70, 90, 115 and 130s), a simple interpolation of the uncertainties obtained at 40, 60, 80, 100 and 150 seconds was made. This accounts for different measuring techniques, data coverage and regularization-schemes in the construction of the maps. Like for model BT04 , we assume for convenience that the errors are Gaussian distributed, but there are too few phase velocity maps to test this hypothesis.

2.2. Parametrization

Azimuthally averaged phase velocities can constrain the five elastic parameters describing radial anisotropy (equation 7). This type of anisotropy occurs when the medium can be characterized by one symmetry axis and this axis points in the radial direction. Only five independent elastic parameters are needed to fully describe this type of medium, and in seismic tomography one often uses the elastic parameters defined by *Love* [1927] : A, C, N, L, and F. These elastic coefficients are directly related to the wave-speed of P-waves traveling either vertically ($V_{PV} = \sqrt{C/\rho}$) or horizontally ($V_{PH} = \sqrt{A/\rho}$), and to the wave-speed of vertically or horizontally polarized S-waves ($V_{SV} = \sqrt{L/\rho}$ or $V_{SH} = \sqrt{N/\rho}$, respectively). Parameter F relates to propagation in other directions (i.e. neither vertical nor horizontal). Seismic anisotropy in a radially anisotropic (or transversely isotropic) medium is then characterized by : $\phi = 1 - C/A$ (describing P-wave anisotropy), $\xi = 1 - N/L$ (describing S-wave anisotropy), $\eta = 1 - F/(A - 2L)$ and one P and one S velocity. For the velocity, some authors choose to work with the velocity of vertically or horizontally propagating waves (or polarized in the case of S-waves), while others choose to use the equivalent isotropic velocities based on the Voigt average [*Voigt*, 1928] isotropic elastic properties : $\mu = (C+A+6L+5N-2F)/15$ and $\kappa = (C+4A-4N+4F)/9$ [*Montagner and Anderson*, 1989]. Note also that the definitions for the anisotropic parameters vary from author to author (for instance some define shear-wave anisotropy as N/L, P-wave anisotropy as C/A and η as $F/(A - 2L)$ [*Gung et al.*, 2003]). In the convention used here, ξ, ϕ and η can be read directly as the amplitude of the anisotropy (e.g. $\xi = 0.04$ would correspond to 4 % of shear-wave anisotropy), and they are thus zero if there is no anisotropy. Negative values of ξ correspond to $V_{SH} > V_{SV}$. Positive values of ϕ correspond to $V_{PH} > V_{PV}$. These anisotropic parameters, widely used in surface wave tomography, differ from the Thomsen parameters [*Thomsen et al.*, 1999; *Mensch and Rasolofosaon*, 1997], which are employed in seismic exploration, and generally in studies dealing with wave front propagation in a transversely isotropic medium [*Favier and Chevrot*, 2003; *Kustowski*, 2007]. The relation between Thomsen and Love parameters can be found in *Babuška and Cara* [1991].

Models are often parametrized in terms of anisotropy parameters, velocity perturbations, and anisotropy parameters [*Gung et al.*, 2003]. We chose, instead, to parametrize the medium directly in terms of elastic parameters A, C, N, L, and F as done in BT04, for comparison purposes. This choice also makes subsequent interpretations in terms of mineral physics data more straightforward than a parametrization in terms of velocities. The sensitivity kernels relating perturbations in phase velocities to perturbations in elastic parameters and density with respect to a reference model (PREM here [*Dziewonski and Anderson*, 1981]) were derived by *Takeuchi and Saito* [1972]. Equation 5 becomes :

$$
\begin{aligned}
{}_k\left(\frac{\delta c}{c}\right)^t_s &= \int_b^a [{}_kK_A(r)\delta A^t_s(r) + {}_kK_C(r)\delta C^t_s(r) \\
&+ {}_kK_N(r)\delta N^t_s(r) + {}_kK_L(r)\delta L^t_s(r) \\
&+ {}_kK_F(r)\delta F^t_s(r) + {}_kK_\rho(r)\delta\rho^t_s(r)]\, dr \qquad (7)
\end{aligned}
$$

where b is the radius of core-mantle boundary and a is the radius of the Earth. For the present research we employed the anisotropic version of PREM, which includes radial anisotropy in the top 220 km of the mantle [*Dziewonski and Anderson*, 1981].

As described in section 1, it is common for seismologists to solve equation 7 only for the best-resolved parameters δN and δL (or $\delta\xi$ and δV_S, depending on the chosen parametrization). Inversions of surface wave data cannot robustly constrain the other parameters because of lower sensitivity and/or because of the existence of large parameter trade-offs. The remaining four parameters are thus often dealt with by using *a priori* petrological constraints so that $\delta lnV_p \propto \delta lnV_s$, $\delta ln\rho \propto \delta lnV_s$, $\delta ln\phi \propto \delta ln\xi$, and $\delta ln\eta \propto \delta ln\xi$. In the work presented here, we solve equation 7 for the two-shear-wave related parameters (δN and δL) and we use scaling factors identical to those employed by *Gung et al.* [2003] to constrain the other parameters : $\delta lnV_p = 0.5\delta lnV_s$, $\delta ln\rho = 0.3\delta lnV_s$, $\delta ln\phi = 1.5\delta ln\xi$, and $\delta ln\eta = 2.5\delta ln\xi$. The scaling factors for the anisotropy parameters are based on computations and results from laboratory experiments [*Montagner and Anderson*, 1989]. The ratio between P-wave and S-wave velocity anomalies is based on values published by *Masters et al.* [2000], and the ratio between density and velocity anomalies is based on the assumption that thermal effects dominate both velocity and density anomalies. We derive the equivalent isotropic V_p and V_s using the Voigt average isotropic elastic properties, as defined above. Proportionality factors between $\delta ln V_p$, $\delta ln V_s$ and $\delta ln\rho$ and between $\delta ln\phi$, $\delta ln\xi$ and $\delta ln\eta$ are converted into relationships between δA, δC, δN, δL, δF, and $\delta\rho$ in order to use a parametrization in terms of elastic parameters as in BT04. Equation 7 becomes :

$$ {}_k\left(\frac{\delta c}{c}\right)^t_s = \int_b^a \left[{}_kK'_N(r)\delta N^t_s(r) + {}_kK'_L(r)\delta L^t_s(r)\right] dr \tag{8} $$

where sensitivity kernels ${}_kK'_N$ and ${}_kK'_L$ are linear combinations of the kernels for A, C, N, L, and F. We also tested the results stability with respect to the ratios between the anisotropic parameters by selecting different values of $\delta ln\phi/\delta ln\xi$ and $\delta ln\eta/\delta ln\xi$.

In order to make meaningful comparisons between models obtained with and without prior scalings, we adopted the same depth parametrization as the one used in BT04 : one isotropic layer between depths of 220 km and 670 km, and two anisotropic layers from 100 km to 220 km depth and from the Moho to 100 km depth. The choice made by *Beghein and Trampert* [2004a] was not based on the depth resolution of the data, but was mainly motivated by computational resources. They needed to reduce the total number of unknows in their problem because forward modeling techniques are more time consuming than traditional inversions. In order to do this and in order to obtain posterior model distributions for the five elastic parameters and density in each layer instead of introducing *a priori* petrological constraints, they used a coarse depth layering. For the purpose of this paper, this coarse parametrization is sufficient but a detailed geodynamical interpretation would clearly need a more refined analysis.

3. The Model Space Search

We applied the Neighbourhood Algorithm (NA) [*Sambridge*, 1999a, b] to the SH coefficients of the phase velocity maps in order to identify the regions of the model space that best fit the data. The NA has been described at length in various publications to which we refer the reader for technical details [*Sambridge*, 1999a, b; *Resovsky and Trampert*, 2002; *Beghein and Trampert*, 2004a]. In brief, it explores the model space to identify regions of relatively low and relatively high misfit, associated with high and low likelihoods, respectively. We thus get an overview of the models compatible with the data rather than choosing one "best" solution with a subjective regularization. The distributions of models obtained are converted into posterior probability density functions (PPDFs), which can be used to assess the robustness and likelihood of the features observed.

Direct search approaches such as the NA are most often employed to solve non-linear problems. This type of problem often has multiple minima and using traditional inverse techniques leads to solutions strongly dependent upon prior assumptions and regularization. Model space search techniques offer a way to obtain robust information on the models without having to introduce explicit *a priori* information or regularization on the model parameters (i.e. $\lambda = 0$ and no $\Delta_{\mathcal{M}}$ used) for a given parameterization, and therefore have great advantages for solving non-linear problems, which often have a non-Gaussian model space.

There are, however, advantages in using these types of techniques to solve linear problems as well. Model distributions are generally assumed to be Gaussian when solving an inverse problem, but this is not necessarily correct as we illustrate in the Results section (Figure 2) of this manuscript. By using a forward modeling method, we do not have to make this assumption as we are able to map the model space and obtain information on its approximate topology. This enables us to directly assess which parameters trade-off with one another, and to explore the entire model space (within selected boundaries), including model null-space, which leads to more accurate posterior model uncertainties. Most linearized inversions give, by construction, a posterior model covariance smaller or equal to the prior covariance by construction [*Tarantola*, 1987]. If the cost function to be minimized has a large valley, that is if there is a large model null-space, the posterior covariance can be seriously underestimated, depending on the prior covariance [*Trampert*, 1998]. This makes both the interpretation and the uncertainty assessment of tomographic models less straightforward than usually thought (see example in *Beghein and Trampert* [2003]). The exploration of the model space enables us to calculate the width of the valley in the cost function (i.e., the width of the individual PPDFs), which is a more realistic representation of the error bars. In addition, by identifying the entire group of models compatible with a data set and obtaining model distributions, we can determine which are the well-defined model features, i.e., which are the properties common to all the good models. This can lead to more meaningful interpretation and integration of the models with results from other fields than interpreting a single model obtained from a regularized inversion.

4. Results

We obtained distributions of models for $(\delta N)_s^t$ and $(\delta L)_s^t$ for spherical harmonic degree s between 0 and 8 ($t = -s, ..., +s$), from which a mean value and a standard deviation can easily be determined. We calculated the rms amplitude and its relative error bar ($d(rms)/rms$) for δN and for δL (Figure 1) in the two anisotropic layers. The rms amplitudes were based on the mean $(\delta N)_s^t$ and $(\delta L)_s^t$ models, and the models standard deviations were used to compute $d(rms)/rms$. We found that the rms amplitudes of the mean models are generaly larger when *a priori* scaling constraints are imposed (Figure 1A). It should be noted that this observation would not necessarily hold if the models were obtained with a traditional inversion method since the regularization imposed tends to reduce model amplitudes, and not necessarily in the same way for L or for N. In Figure 1B we displayed $d(rms)/rms$, which represents the size of the error bars on the rms relative to the size of the mean model. We see that the relative uncertainty on the rms amplitude is systematically smaller (by approximately a factor two) for models obtained with *a priori* constraints. The reduction in the size of the posterior model uncertainties when *a priori* information is included is consistent with the formalism of *Jackson and Matsu'ura* [1985], who demonstrated that when prior information is used to solve an inverse problem both the observations and the prior information contribute to the resolution matrix. They also showed that strong prior information can compensate the low resolution one would obtain from observations alone. This is illustrated in Figure 2, as explained below.

In Figure 2, we display examples of how the introduction of *a priori* petrological constraints affect the posterior model distributions. The distributions of model parameters shown were obtained using the degree zero of the phase velocity maps SH expansion ($s = t = 0$). We see that the posterior model distributions obtained without imposing prior constraints (BT04 models, in grey) can depart significantly from a Gaussian, but the introduction of prior information can strongly modify the shape of these distributions, which then become more Gaussian-like. For example, for parameter dN_0^0 in the bottom layer the data alone (thus without prior scalings) tend to slightly favor a solution with $dlnN_0^0 = 0.05$ but with very large uncertainties. Because the model uncertainties are so large, the weighted mean is much smaller (≈ 0.01) than what one would pick as the most likely value (≈ 0.05). The fact that the mean and the most likely values for dN_0^0 are so different demonstrates that the model distribution is wide and not Gaussian. However, we see that including prior scaling relationships reduces the range of solutions and the distribution becomes Gaussian-like with a positive mean value of approximately 0.02. Thus in this case, both prior information and data favor a positive $dlnN_0^0$, but with a different level of certainty.

Figure 2 also demonstrates that in some cases the introduction of prior information can change the solution dramatically. This is illustrated by dL_0^0 in the bottom layer : The BT04 model distribution is wide and not Gaussian, with a negative peak. However, when imposing prior constraints, not only does the model uncertainty become smaller, but the peak of the distribution shifts toward clearly positive values, in contradiction with the direction towards which the data were pushing the solution in BT04. If this type of behavior were to occur for a large number of spherical harmonics and elastic parameters, it could be a problem if the prior information is not justified as the solution and the resolution of the parameter are driven by the prior information and not by the data themselves. Note that a similar observation can be made for dN_0^0 in the top layer, but with a less strong change when prior information in introduced.

The reader will also notice that the most likely solution for dN_0^0 in the bottom layer is at the edge of the model space. In the case where prior constraints are imposed, increasing the size of the model space would likely provide a solution that is not at the model space boundary anymore because the $(\delta N)_0^0$ and $(\delta L)_0^0$ parameters are well-resolved. However, in the case of the BT04 models, dN and dL trade-off with some of the other elastic parameters (e.g., $d\rho$). Experience with previous studies of this kind [*Beghein et al.*, 2002; *Beghein and Trampert*, 2003, 2004a, b; *Beghein et al.*, 2006, 2008] showed us that changing the boundary for one parameter to better locate its peak value can change the most likely value of another parameter if the two parameters trade-off strongly with one another. In such cases, expanding the model space boundaries is not necessarily helpful. In addition, one needs to keep in mind that our calculations of phase velocity perturbations for a given Earth model are based on perturbation theory. We cannot therefore increase the model space size indefinitely without violating the conditions of applications of the theory behind those calculations. We thus decided to maintain the range within which we sample the model space identical to the ones used in the BT04 models even though the solution for dL_0^0 in the top layer peaks at the edge. The reader should keep in mind that the results presented here are valid for a particular parametrization and set of basis functions.

The degree zero ξ likelihoods that result from the dN_0^0 and dL_0^0 distributions (Figure 2B) display an identical behavior, with smaller uncertainties when prior constraints are used. In the top layer, the position of the peaks with respect to PREM (shown by the vertical line) is not strongly affected by the use of prior information, but a noticeable change is visible in the bottom layer, likely because data sensitive to deeper structure have tend to have larger uncertainties and are more affected by prior constraints.

Figures 3 to 5 illustrate how the choice of the value of $dln\eta/dln\xi$ and of $dln\phi/dln\xi$ influences the posterior distributions. The values found in the literature ($dln\eta/dln\xi =$

2.5 and of $dln\phi/dln\xi = 1.5$) are based on a study by *Montagner and Anderson* [1989] who investigated the correlations between anisotropic parameters for different orientations and mineralogical and petrological models of the upper mantle. Some authors, however, neglect $d\eta$ and $d\phi$ and perform inversions for S-wave velocity and anisotropy only, which is equivalent to $dln\eta/dln\xi = dln\phi/dln\xi = 0$ [*Maggi et al.*, 2006; *Marone and Romanowicz*, 2007b]. To determine how shear-wave anisotropy models are sensitive to the values of these ratios, we performed model space searches for parameters at degree zero with different values of $dln\eta/dln\xi$ and of $dln\phi/dln\xi$. In Figure 3, $dln\eta/dln\xi$ and of $dln\phi/dln\xi$ are assumed to be zero. We see that this assumption affects the distributions only very slightly in the top layer, and that the distributions differ more in the deeper layer. We do not have any estimates of uncertainties on these ratios. We nevertheless tested the sensitivity of the results to changes in $dln\eta/dln\xi$ and $dln\phi/dln\xi$ by changing the sign of each ratio (Figure 4) and by increasing each of the two ratios by a factor two (Figure 5). From these tests, we see that changing the sign of $dln\eta/dln\xi$ does not significantly affect the distributions, but changing the sign of $dln\phi/dln\xi$ does have a large effect on $(\delta N)^t_s$, $(\delta L)^t_s$, and ξ. Changing the sign of $dln\phi/dln\xi$ corresponds to having opposite fast directions for P- and S-waves, i.e. the fast direction for S-waves would be the slow direction for P-waves. This is not a scenario that is usually considered in the literature, but it cannot be completely dismissed. Indeed, *Mainprice et al.* [2000] showed that compositional changes (e.g. an increase in pyroxenes) can affect the fast direction for P-waves while S-wave anisotropy remains unchanged. This could affect the sign of the P- to S-anisotropy ratio. Finally, Figure 5 shows that increasing either $dln\eta/dln\xi$ or $dln\phi/dln\xi$ by a factor two changes the shape and peak position of the $(\delta N)_s^t$ and $(\delta L)_s^t$ distributions but does not affect the resulting ξ distributions significantly.

Despite the difference in the rms amplitudes (Figure 1), changes in the amplitude, and sometimes in the sign of some parameters (Figure 2), the global correlation between the mean models obtained with and without scaling relationships is high. The values calculated for the correlation coefficients are : 0.97 and 0.91 for δL in the top and bottom layer, respectively, and 0.96 and 0.95 for δN in the top and bottom layer, respectively (including all SH between 0 and 8). This shows that the general features of the weighted mean L and N models are not strongly affected by the introduction of *a priori* petrological constraints. The weighted mean model does not, however, necessarily correspond to the best data fitting model as it can differ from the peak of the distribution (or most likely solution) if it is not Gaussian, as seen in Figure 2. We therefore also calculated the global correlation between the two most likely models (Figure 2) and found high correlation values of 0.91 and 0.93 for dN in the top and bottom layer, respectively, and 0.96 and 0.87 for dL in the top and bottom layer, respectively. Thus, whether we consider the mean or the most likely models, the introduction of prior petrological constraints does not dramatically affect the geographical distribution of the anisotropy anomalies.

From the weighted mean $(\delta N)_s^t$ and $(\delta L)_s^t$ at degrees 0 through 8, we constructed maps for dL and dN (using equation 4). Using the Voigt average (as defined in section 2.2), we then constructred maps of shear-wave velocity and shear-wave anisotropy anomalies $dlnV_s = dV_s/V_s$ and $d\xi = \xi - \xi_p$ where ξ_p is the shear-wave anisotropy in PREM. Because ξ_p is negative, negative values of $d\xi$ correspond to a larger anisotropy than in PREM (with $V_{SH} > V_{SV}$). Note that in the case with prior constraints, the mean and most likely models almost coincide since the model distributions are approximately Gaussian for most parameters. Figure 6 represents the reconstructed $d\xi$ models. On the left-hand-side of the figure, we represented the "mean models", reconstructed based on the weighted mean values of the $(\delta N)_s^t$ and $(\delta L)_s^t$ distributions. We see in panels (A) and (C) that the main features of the mean models obtained with and without petrological constraints are very similar, in agreement with the high correlation coefficients calculated above. Some changes occur in the amplitude of the anisotropy anomalies. We observe larger amplitudes in the top 100 km when a scaling is imposed (e.g. positive anomaly in the central Pacific, negative anomalies north-west of India, near the Tonga subduction zone, and in the north western Pacific). On the contrary, between depths of 100 and 220 km the negative anomalies appear stronger when no prior is imposed, as seen in the central Pacific. Both models explain the data within uncertainties, with a χ-misfit of 0.6 when prior information is included, and $\chi = 0.82$ when all elastic parameters are allowed to vary independently. Note that we performed a statistical F-test [*Bevington and Robinson*, 1992] in order to determine whether these two mean models were equivalent. The test returned a 97% probability that the models are equivalent, which confirms that the comparison of their misfits and the calculation of their correlation is justified and fair.

As explained above, the weighted mean model is not meaningful by itself, especially when the model space is not Gaussian, and we need to consider it together with its associated uncertainties. Besides looking at model distributions or the relative rms uncertainty (Figure 1B), a way to estimate model uncertainty is by comparing the mean model and the "mean robust models" (right-hand side of Figure 6). The "mean robust model" is constructed from the mean model and is defined as follows : the mean robust model is constructed using the mean value $\overline{\delta m}$ of $(\delta N)_s^t$ or $(\delta L)_s^t$ if the standard deviation $\sigma(\overline{\delta m})$ is smaller than $\overline{\delta m}$, and it uses $\overline{\delta m} = 0$ if $\sigma(\overline{\delta m}) > \overline{\delta m}$. The mean model and the mean robust model are thus identical if all $(\delta N)_s^t$ and $(\delta L)_s^t$ have uncertainties smaller than than their mean value, i.e. if all SH coefficients are non-zero and well-resolved. The two models differ where model parameters have large uncertainties. We can therefore see the mean robust model as the robust part of the mean model, as it is constituted of the best-constrained $(\delta N)_s^t$ and $(\delta L)_s^t$ only, and their comparison gives a qualitative estimate of which features are well-resolved. Note that the mean and the mean robust models do not necessarily explain the data equivalently well, as deviations from zero might be required by the data for several parameters even if the range of possible values is large. In addition, one should keep in mind, however, that the well-resolved geometry obtained from surface wave data alone is not necessarily the "true" model. The family of models compatible with the selected surface wave dataset should, ideally, be tested against other types of data before interpreting the observed features.

When comparing the mean model and the mean robust model in the case where prior constraints are imposed (Figure 6(A) and (B)), we do not observe any significant differences in pattern or amplitude. This is because most coefficients $(\delta N)_s^t$ and $(\delta L)_s^t$ have small uncertainties (see also Figure 1). However, when no petrological information is introduced discrepancies are visible between the mean model and the mean robust model in the BT04 study (Figure 6(C) and (D)) due to larger model uncertainties without prior information. Some of the anomalies seen in the mean model (Figure 6(C)) are not as well visible in the mean robust model (Figure 6(D)). For instance, this is the case in the bottom layer of Figure 6(C) for the positive $d\xi$ observed north of Indonesia and the negative $d\xi$ along the west coast in North America. These features are the ones that have the largest error bars. On the contrary, model features that are found in the mean robust model are well-constrained by the seismic data alone since no prior was introduced. This is the case in the bottom layer for the large-scale positive $d\xi$ along ocean ridges and the western US coast and for the negative anomaly in the Pacific ocean, and in the top layer for the positive $d\xi$ in the Pacific and the negative $d\xi$ beneath asia. On the contrary, the features of the mean robust model obtained in this study (Figure 6(B)) are resolved by a combination of constraints from the data and constraints from the prior information. By comparing the mean robust models obtained with (B) and without (D) prior scaling, we can thus assess which are the model features that appear well-constrained when prior is introduced but that are in fact dominated by it and not constrained by the seismic data. This is the case, for example, for the $d\xi > 0$ signal north of Indonesia and $d\xi < 0$ along the western US in the bottom layer (Figure 6(B)).

Since PREM includes radial anisotropy in the top 220 km of the mantle, the total anisotropy ξ differs from the perturbation $d\xi$ with respect to the reference model PREM. Besides, ξ is a physical quantity that is more easily interpreted and more directly related to mantle deformation than $d\xi$. In Figure 7 we thus plotted the mean and most likely ξ models. As already discussed for $d\xi$, the mean models obtained with and without scalings differ very little from one another. In both cases, the dominant signal in the top 100 km shows $V_{SH} > V_{SV}$, likely reflecting horizontal plate motion, as commonly seen in other studies of radial anisotropy [*Nettles and Dziewonski*, 2008]. In that layer, we also see that some areas display stronger anisotropy (with negative ξ) than others : at the boundary between North America and the Pacific plate, between the Pacific and

Australian plates, in Asia, and along ocean ridges. In the bottom layer, strong features common to both models are $V_{SV} > V_{SH}$ beneath part of Asia, and $V_{SH} > V_{SV}$ south of India, near the Indian mid-ocean ridge. Because these features are independent of whether prior constraints are imposed, we can conclude that they are robust and mostly constrained by the phase velocity data. The main differences between the two mean models lie in the amplitude of the anisotropy in the middle of the Pacific ocean in both layers. Figure 7(C) also shows that the major change observed between the most likely BT04 model and the two mean models lies in the amplitude of the anisotropy, which is significantly larger for the most likely model. This is especially visible in the top layer at several plate boundaries and in the middle of the Pacific, and in the bottom layer beneath Asia, south of India, and in the middle of the Pacific ocean. These differences in amplitude between weighted mean and most likely models reflect the fact that the model space is *a priori* not Gaussian. It also reinforces the importance of not just looking at one possible best data fitting model, but at the family of models that can explain the data. In addition, one should keep in mind that the most likely BT04 model is not necessarily more representative of the "real" Earth than the mean BT04 model or than the model obtained with prior information, and that the models should ideally be tested against other types of data before interpretation.

Another way of determining which are the dominant model features in a model is by taking a statistical point of view and looking at model distributions. The ensemble of models that explain the data may have well defined, robust properties, common to most best data-fitting models and that can be interpreted confidently. We decided to adopt the method described by *Beghein and Trampert* [2004a] to display distributions of models in tectonic regions of different ages. This method consists in drawing random values of δN_s^t and δL_s^t from their posterior 1D marginal distributions for each spherical harmonic degree $s = 0 - 8$ and azimuthal order $t = -s, ..., +s$. Then we calculate the resulting N and L models, and reconstruct ξ and $dlnV_s$ on a grid of points (θ, ϕ). For each ξ and $dlnV_s$ model generated this way, we bin the ξ and $dlnV_s$ values, and average them over specific tectonic regions such as cratons, continental platforms, young oceans, old oceans, etc. Histograms are then constructed for a given region by accumulating the averaged values generated randomly. These histograms represent thus the distribution of data-compatible values of ξ and $dlnV_s$, averaged over a given area, and do not account for variations within the area considered. The resulting likelihood distributions of models are shown in Figure 9 for ξ and in Figure 8 for $dlnV_s$. We see that the general age-dependence of the $dlnV_s$ distributions is not dependent on the use of petrological constraints : In both cases, old oceans and cratons are most likely characterized by higher velocity anomalies than younger oceans or tectonically active areas, respectively. This is in general agreement with previous models (e.g. *Nishimura and Forsyth* [1989]; *Ritzwoller et al.* [2004]). The spread of the distributions is larger when no prior constraint is imposed, which is to be expected since this is true for the individual elastic parameters, as shown in Figure 2.

While the age-dependence of seismic wave velocities in oceanic lithosphere is well-accepted in the community, it is not clear whether a similar behavior can be found in seismic anisotropy. *Montagner* [1985] found an increase in shear-wave polarization anisotropy with the age of the ocean floor, with $V_{SH} > V_{SV}$ down to a depth of 300 km. *Nishimura and Forsyth* [1989] found a similar result with a rapid increase in shear-wave anisotropy in the first 20 Ma until an apparently constant value is reached for older oceans. Similarly, the BT04 results suggested an age-dependence of the depth extent of S-wave anisotropy in oceanic regions, and a likely difference in amplitude of the anisotropy between old and young oceans, but with large uncertainties. Such a behavior was also reported based on azimuthal anisotropy [*Debayle et al.*, 2005; *Maggi et al.*, 2006], suggesting an increase in the lithosphere-asthenosphere transition depth as the oceanic plate cools down and thickens. Here, we see that, with or without prior constraints, the peaks of the distributions show an age-dependence of the anisotropy (Figure 9), and a faster decrease with depth below young regions than below older regions, which is compatible with the idea that the lithospheric thickness as seen with radial anisotropy increases with the age of the ocean floor. The distributions are narrower when prior constraints are imposed, reinforcing the difference between the strength of the anisotropy in old and in young oceanic lithosphere. Similarly, when imposing petrological constraints, the likelihood of having a difference between ξ in cratons and in younger continental regions is increased compared to models where no prior is imposed.

5. Conclusions

The aim of this study was to analyze in details the effect of *a priori* petrological constraints on models of uppermost mantle shear wave radial anisotropy. In order to isolate the effects of petrological constraints from the effects of explicit regularization, which cannot easily be distinguished with traditional inversion methods, we used a forward modeling approach and compared models obtained with and without prior petrological constraints. We showed that model distributions are not necessarily Gaussian *a priori* but that imposing petrological constraints can force the models to follow a Gaussian-like posterior distribution in addition to reducing posterior model uncertainties, in agreement with inverse theory [*Jackson and Matsu'ura*, 1985]. Our results demonstrated that these prior constraints do not significantly affect the geometry of large-scale uppermost mantle radial anisotropy models. The models obtained with and without prior information are similar, highly correlate with one another, and explain the data within uncertainties. Differences were found between maps of most likely shear-wave anisotropy, but they mostly lie in the amplitude of the anomalies and not in the pattern of the anisotropy.

The method employed enabled us to explore the model space, including the null-space, and obtain reliable model uncertainties, which then could be used to assess the best-resolved model features. In addition, we could determine which model features were constrained by the surface wave data alone and which were dominated by the prior introduced. We found, for instance, that the anisotropy anomalies detected along ocean ridges and in the central Pacific were well-constrained, with small uncertainties, by the surface wave data alone. Finally, we demonstrated that the age-dependence of the amplitude and depth extent of velocity anomalies under continents and under oceans is independent of whether petrological constraints are introduced or not. It is therefore a well-defined signal constrained by seismic data alone. Similarly, we find an age-related signal for shear-wave anisotropy under continents and oceans (confirming the findings of *Nishimura and Forsyth* [1989]), but with larger uncertainties when no prior is imposed. We thus can conclude that global shear-wave velocity and anisotropy model features are not strongly affected by the introduction of prior constraints, but regional amplitude effects can be more important.

Acknowledgments. C.B. thanks M. Sambridge for making his Neighbourhood algorithm freely available and J. Trampert for his global surface wave dispersion data set. Paul

Davis kindly read and commented on a first draft of this manuscript. Two anonymous reviewers helped improve the manuscript.

References

Babuška, V., and M. Cara (1991), *Seismic Anisotropy in the Earth*, Springer.

Becker, T., J. Kellogg, G. Ekstrom, and R. O'Connell (2003), Comparison of azimuthal seismic anisotropy from surface waves and finite strain from global mantle-circulation models, *Geophys. J. Int.*, *155*, 696–714.

Becker, T., B. Kustowski, and G. Ekstrom (2008), Radial seismic anisotropy as a constraint for upper mantle rheology, *Earth and Planetary Science Letters*, *267*(1-2), 213–227, doi:10.1016/j.epsl.2007.11.038.

Becker, T. W. (2008), Azimuthal seismic anisotropy constraints net rotation of the lithosphere, *Geophys. Res. Lett.*, *35*, L05,303, doi:10.1029/2007GL032928.

Becker, T. W., S. Chevrot, V. Schulte-Pelkum, and D. K. Blackman (2006a), Statistical properties of seismic anisotropy predicted by upper mantle geodynamic models, *Journal of Geophysical Research-Solid Earth*, *111*, B08,309, doi:10.1029/2005JB004095.

Becker, T. W., V. Schulte-Pelkum, D. K. Blackman, J. B. Kellogg, and R. J. O'Connell (2006b), Mantle flow under the western united states from shear wave splitting, *Earth and Planetary Science Letters*, *247*, 235–251, doi:10.1016/j.epsl.2006.05.010.

Beghein, C., and J. Trampert (2003), Robust normal mode constraints on inner-core anisotropy from model space search, *Science*, *299*, 552–555.

Beghein, C., and J. Trampert (2004a), Probability density functions for radial anisotropy from fundamental mode surface wave data and the neighbourhood algorithm, *Geophys.*

J. Int., *157*, 1163–1174, doi:10.1111/j.1365-246X.2004.02235.x.

Beghein, C., and J. Trampert (2004b), Probability density functions for radial anisotropy: implications for the upper 1200 km of the mantle, *Earth and Planetary Science Letters*, *217*, 151–162, doi:10.1016/S0012-821X(03)00575-2.

Beghein, C., J. Resovsky, and J. Trampert (2002), P and s tomography using normal-mode and surface waves data with a neighbourhood algorithm, *Geophys. J. Int.*, *149*, 646–658.

Beghein, C., J. Trampert, and H. van Heijst (2006), Radial anisotropy in seismic reference models of the mantle, *Journal of Geophysical Research-Solid Earth*, *111*, B02,303, doi: 10.1029/2005JB003728.

Beghein, C., J. Resovsky, and R. D. van der Hilst (2008), The signal of mantle anisotropy in the coupling of normal modes, *Geophys. J. Int.*, *175 (3)*(1209-1234), doi:10.1111/j.1365–246X.2008.03,970.x.

Bevington, P., and D. Robinson (1992), *Data Reduction and Error Analyses for the Physical Sciences*, McGraw-Hill, New York.

Boschi, L., and A. Dziewonski (1999), High-and low-resolution images of the earth's mantle: Implications of different approaches to tomographic modeling, *Journal of Geophysical Research*, *104* (B11), 25,567–25,594.

Boschi, L., and G. Ekström (2002), New images of the earth's upper mantle from measurements of surface wave phase velocity anomalies, *Journal of Geophysical Research-Solid Earth*, *107*(B4), 2059, doi:10.1029/2000JB000059.

Bozdag, E., and J. Trampert (2008), On crustal corrections in surface wave tomography, *Geophys. J. Int.*, *172*, 1066–1082, doi:10.1111/j.1365-246X.2007.03690.x.

Carannante, S., and L. Boschi (2005), Databases of surface wave dispersion, *Ann Geophys-Italy*, *48*, 945–955.

Chen, M., and J. Tromp (2007), Theoretical and numerical investigations of global and regional seismic wave propagation in weakly anisotropic earth models, *Geophys. J. Int.*, *168*, 1130–1152, doi:10.1111/j.1365-246X.2006.03218.x.

Dahlen, F., and J. Tromp (1998), *Theoretical Global Seismology*, Princeton University Press, Princeton, NJ.

Debayle, E., B. Kennett, and K. Priestley (2005), Global azimuthal seismic anisotropy and the unique plate-motion deformation of australia, *Nature*, *433*, 509–512, doi:10.1038/nature03247.

Dziewonski, A., and D. Anderson (1981), Preliminary reference earth model, *Physics of the Earth and Planetary Interiors*, *25*, 297–356.

Edmonds, A. (1960), *Angular Momentum in Quantum Mechanics*, Princeton University Press, Princeton, NJ.

Ekström, G., and A. Dziewonski (1998), The unique anisotropy of the pacific upper mantle, *Nature*, *394*, 168–172.

Ekström, G., J. Tromp, and E. Larson (1997), Measurements and global models of surface wave propagation, *Journal of Geophysical Research-Solid Earth*, *102*, 8137–8157.

Favier, N., and S. Chevrot (2003), Sensitivity kernels for shear wave splitting in transverse isotropic media, *Geophys. J. Int.*, *153*(1), 213–228.

Fouch, M., and K. Fischer (1996), Mantle anisotropy beneath northwest pacific subduction zones, *Journal of Geophysical Research-Solid Earth*, *101*, 15,987–16,002.

Gung, Y., M. Panning, and B. Romanowicz (2003), Global anisotropy and the thickness of continents, *Nature*, *422*, 707–711, doi:10.1038/nature01559.

Jackson, D. (1979), The use of a priori data to resolve non-uniqueness in linear inversion, *Geophys. J. R. A. S.*, *57*, 137–158.

Jackson, D., and M. Matsu'ura (1985), A bayesian approach to nonlinear inversion, *J. Geophys. Res.*, *90*(B1), 581–591.

Karato, S., and M. Toriumi (1989), *Seismic anisotropy: mechanisms and tectonic implications*, pp. 393–422, Oxford Univ. Press, Oxford, UK.

Kendall, J., S. Karato, A. Forte, R. Liebermann, G. Masters, and L. Stixrude (2000), *Seismic anisotropy in boundary layers of the mantle*, vol. 117, pp. 133–159, AGU.

Kustowski, B. (2007), Modeling the anisotropic shear-wave velocity structure in the earth's mantle on global and regional scales, *PhD thesis*, p. 218.

Kustowski, B., A. M. Dziewonski, and G. Ekström (2007), Nonlinear crustal corrections for normal-mode seismograms, *Bulletin of the Seismological Society of America*, *97*, 1756–1762, doi:10.1785/0120070041.

Laske, G., and G. Masters (1996), Constraints on global phase velocity maps from long-period polarization data, *Journal of Geophysical Research-Solid Earth*, *101*, 16,059–16,075.

Lay, T., Q. Williams, E. Garnero, L. Kellogg, and M. Wysession (1998), Seismic wave anisotropy in the d" region and its implications, *Geodynamics, The core-mantle boundary region*, *28*, 299–318.

Lévêque, J., and M. Cara (1985), Inversion of multimode surface-wave data - evidence for sub-lithospheric anisotropy, *Geophys. J. R. A. S.*, *83*(3), 753–773.

Love, A. (1927), *A treatise on the mathematical theory of elasticity*, Cambridge Univ. Press, Cambridge, UK.

Maggi, A., E. Debayle, K. Priestley, and G. Barruol (2006), Azimuthal anisotropy of the pacific region, *Earth and Planetary Science Letters*, *250*, 53–71, doi: 10.1016/j.epsl.2006.07.010.

Mainprice, D., G. Barruol, and W. B. Ismail (2000), The seismic anisotropy of the earth's mantle: From single crystal to polycrystal, *Geohysical Monograph - Earth's deep interior: Mineral physics and tomography from the atomic to the global scale.*, *117*, 237–264.

Marone, F., and B. Romanowicz (2007a), Non-linear crustal corrections in high-resolution regional waveform seismic tomography, *Geophys. J. Int.*, *170*, 460–467, doi: 10.1111/j.1365-246X.2007.03399.x.

Marone, F., and B. Romanowicz (2007b), The depth distribution of azimuthal anisotropy in the continental upper mantle, *Nature*, *447*, 198–U4, doi:10.1038/nature05742.

Marone, F., Y. Gung, and B. Romanowicz (2007), Three-dimensional radial anisotropic structure of the north american upper mantle from inversion of surface waveform data, *Geophys. J. Int.*, *171*(1), 206–222, doi:10.1111/j.1365-246X.2007.03465.x.

Masters, G., G. Laske, H. Bolton, and A. Dziewonski (2000), The relative behavior of shear velocity, bulk sound speed, and compressional velocity in the mantle: Implications for chemical and thermal structure, in *Earth's Deep Interior*, *AGU Monograph*, vol. 117, edited by S. Karato, A. Forte, R. Liebermann, G. Masters, and L. Stizrude, AGU, Washington DC.

Mensch, T., and P. Rasolofosaon (1997), Elastic-wave velocities in anisotropic media of arbitrary symmetry-generalization of thomsen's parameters epsilon, delta and gamma, *Geophys. J. Int.*, *128*(1), 43–64.

Montagner, J. (1985), Seismic anisotropy of the pacific-ocean inferred from long-period surface-waves dispersion, *Physics of the Earth and Planetary Interiors*, *38*, 28–50.

Montagner, J. (1986), Regional 3-dimensional structures using long-period surface-waves, *Ann Geophys B-Terr P*, *4*, 283–294.

Montagner, J., and D. Anderson (1989), Petrological constrants on seismic aanisotropy, *Physics of the Earth and Planetary Interiors*, *54*(1-2), 82–105.

Montagner, J., and B. Kennett (1996), How to reconcile body-wave and normal-mode reference earth models, *Geophys. J. Int.*, *125*(1), 229–248.

Mooney, W., G. Laske, and T. Masters (1998), Crust 5.1: A global crustal model at 5° x 5°, *J. Geophys. Res.*, *103*(B1), 727–747.

Nettles, M., and A. M. Dziewonski (2008), Radially anisotropic shear velocity structure of the upper mantle globally and beneath north america, *Journal of Geophysical Research-Solid Earth*, *113*, B02,303, doi:10.1029/2006JB004819.

Nishimura, C., and D. Forsyth (1989), The anisotropic structure of the upper mantle in the pacific, *Geophys. J. Int.*, *96*(2), 203–229.

Panning, M., and B. Romanowicz (2004), Inferences on flow at the base of earth's mantle based on seismic anisotropy, *Science*, *303*(351), 351–353, doi:10.1126/science.1091524.

Panning, M., and B. Romanowicz (2006), A three-dimensional radially anisotropic model of shear velocity in the whole mantle, *Geophys. J. Int.*, *167*, 361–379, doi:10.1111/j.1365-246X.2006.03100.x.

Resovsky, J., and J. Trampert (2002), Reliable mantle density error bars: an application of the neighbourhood algorithm to normal-mode and surface wave data, *Geophys. J.*

Int., *150*, 665–672.

Resovsky, J., and J. Trampert (2003), Using probabilistic seismic tomography to test mantle velocity-density relationships, *Earth and Planetary Science Letters*, *215*, 121–134, doi:10.1016/S0012-821X(03)00436-9.

Resovsky, J., J. Trampert, and R. van der Hilst (2005), Error bars for the global seismic q profile, *Earth and Planetary Science Letters*, *230*, 413–423, doi: 10.1016/j.epsl.2004.12.008.

Ritzwoller, M., N. Shapiro, and S. Zhong (2004), Cooling history of the pacific lithosphere, *Earth and Planetary Science Letters*, *226*(1-2), 69–84.

Sambridge, M. (1999a), Geophysical inversion with a neighbourhood algorithm - ii. appraising the ensemble, *Geophys. J. Int.*, *138*(3), 727–746.

Sambridge, M. (1999b), Geophysical inversion with a neighbourhood algorithm - i. searching a parameter space, *Geophys. J. Int.*, *138*(2), 479–494.

Silver, P., and W. Holt (2002), The mantle flow field beneath western north america, *Science*, *295*(5557), 1054–1057.

Takeuchi, H., and M. Saito (1972), Seismic surface waves, in *Methods Computational Physics*, vol. 11, pp. 217–295, Academic Press, New York.

Tanimoto, T. (1986), Free oscillations of a slightly anisotropic earth, *Geophys. J. R. A. S.*, *87*, 493–517.

Tarantola, A. (1987), *Inverse Problem Theory, Methods for Data Fitting and Model Parameter Estimation*, Elsevier, New York.

Thomsen, L., I. Tsvankin, and M. Mueller (1999), Coarse-layer stripping of vertically variable azimuthal anisotropy from shear-wave data, *Geophysics*, *64*(4), 1126–1138.

Trampert, J. (1998), Global seismic tomography: the inverse problem and beyond, *Inverse Problems*, *14* (3), 371–385.

Trampert, J., and H. van Heijst (2002), Global azimuthal anisotropy in the transition zone, *Science*, *296*, 1297–1299.

Trampert, J., and J. Woodhouse (1995), Global phase velocity maps of Love and Rayleigh waves between 40 and 150 seconds, *Geophys. J. Int.*, *122*, 675–690.

Trampert, J., and J. Woodhouse (1996), High reolsution global phase velocity distributions, *Geophys. Res. Lett.*, *23*, 21–24.

Trampert, J., and J. Woodhouse (2001), Assessment of global phase velocity models, *Geophys. J. Int.*, *144*, 165–174.

Trampert, J., and J. Woodhouse (2003), Global anisotropic phase velocity maps for fundamental mode surface waves between 40 and 150 s, *Geophys. J. Int.*, *154*, 154–165.

van Heijst, H., and J. Woodhouse (1999), Global high-resolution phase velocity distributions of overtone and fundamental-mode surface waves determined by mode branch stripping, *Geophys. J. Int.*, *137*, 601–620.

Voigt, W. (1928), *Lehrbuch der Kristallphysik*, Teubner, Leipzig.

Wong, Y. (1989), Upper mantle heterogeneity from phase and amplitude data of mantle waves, Ph.D. thesis, Harvard Univ., Cambridge, Mass.

Woodhouse, J., and A. Dziewonski (1984), Mapping the upper mantle: Three-dimensional modeling of earth structure by inversion of seismic waveforms, *Journal of Geophysical Research*, *89* (B7), 5953–5986.

Wookey, J., J. Kendall, and G. Barruol (2002), Mid-mantle deformation inferred from seismic anisotropy, *Nature*, *415*, 777–780.

Zhang, Y., and T. Tanimoto (1992), Ridges, hotspots and their interaction as observed in seismic velocity maps, *Nature*, *355*(6355), 45–49.

Zhou, Y., G. Nolet, F. Dahlen, and G. Laske (2006), Global upper-mantle structure from finite-frequency surface-wave tomography, *Journal of Geophysical Research-Solid Earth*, *111*(B4).

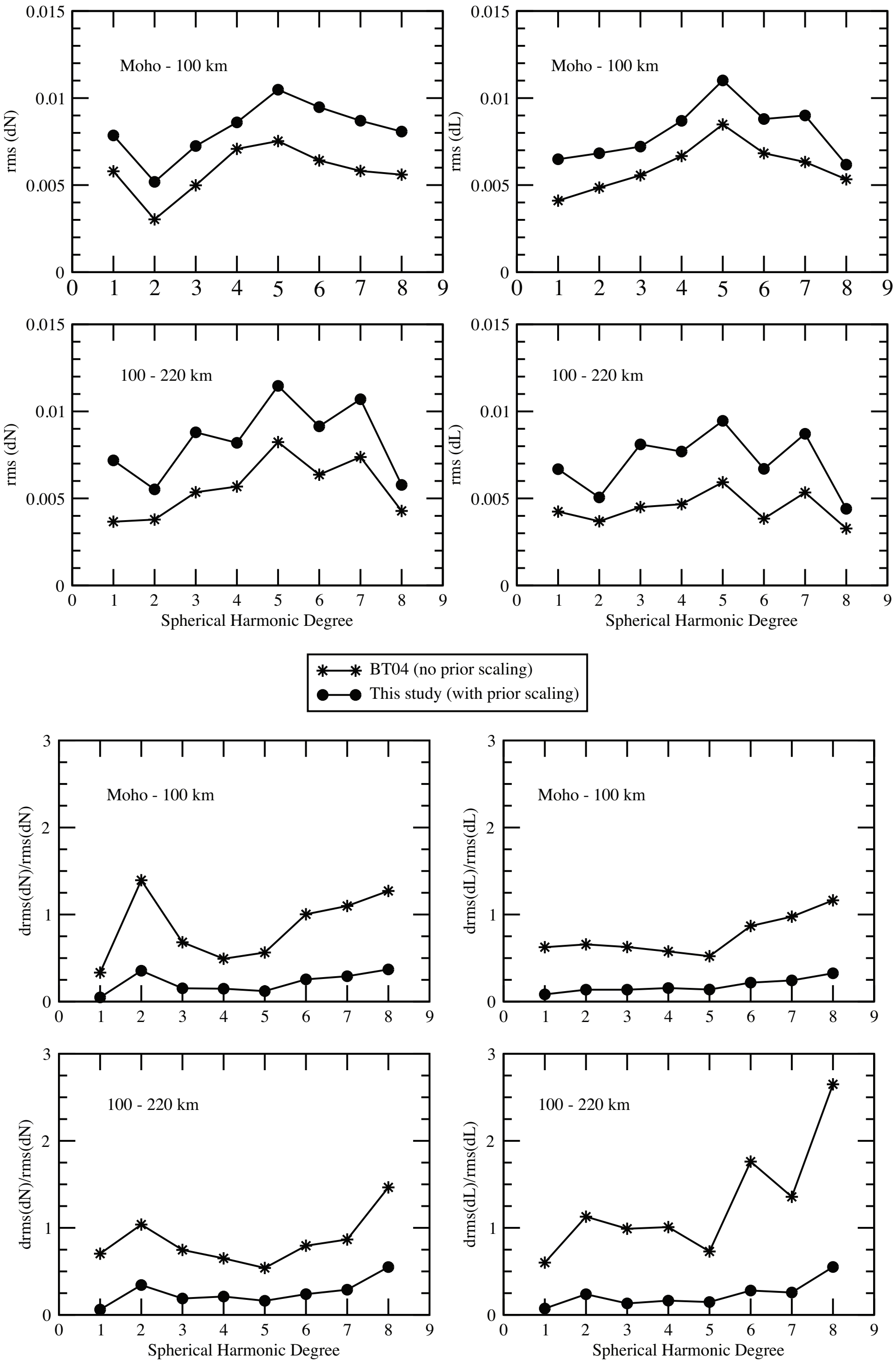

Figure 1. (A) Root mean square amplitude of perturbations in elastic parameters L and N as a function of spherical harmonic degree, in the BT04 models and in a case where no petrological constraints are imposed *a priori*; (B) Relative uncertainty on the rms amplitude of the mean L and N model.

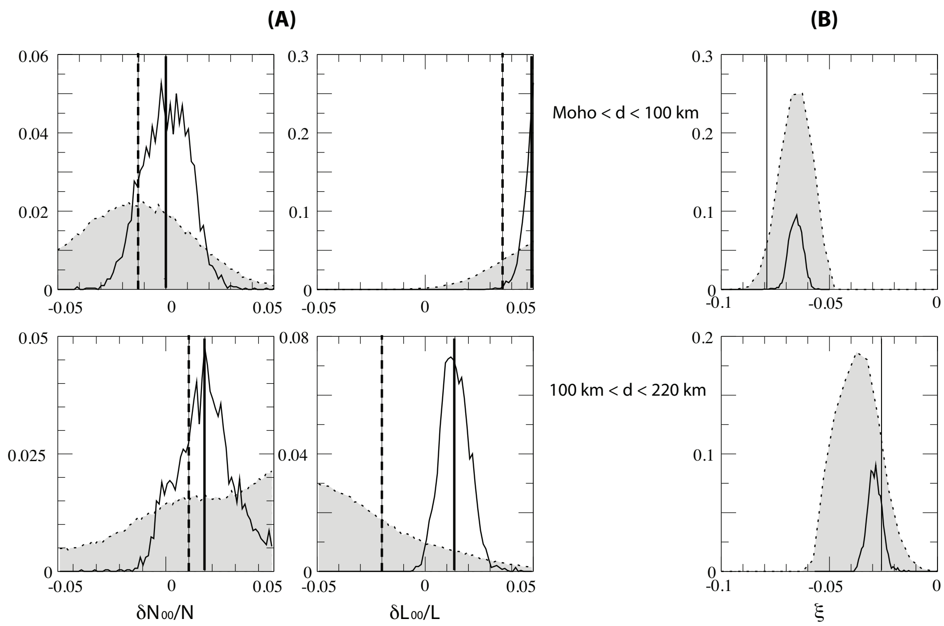

Figure 2. Examples of the effect of prior scalings on (A) the δN_s^t, δL_s^t distributions at spherical harmonic degree s and order t equal to zero, and (B) the resulting ξ distributions . Note that these distributions are not normalized. In (A), the vertical lines correspond to the weighted mean value as output by the NA. In (B) the vertical lines correspond to the value of ξ in PREM.

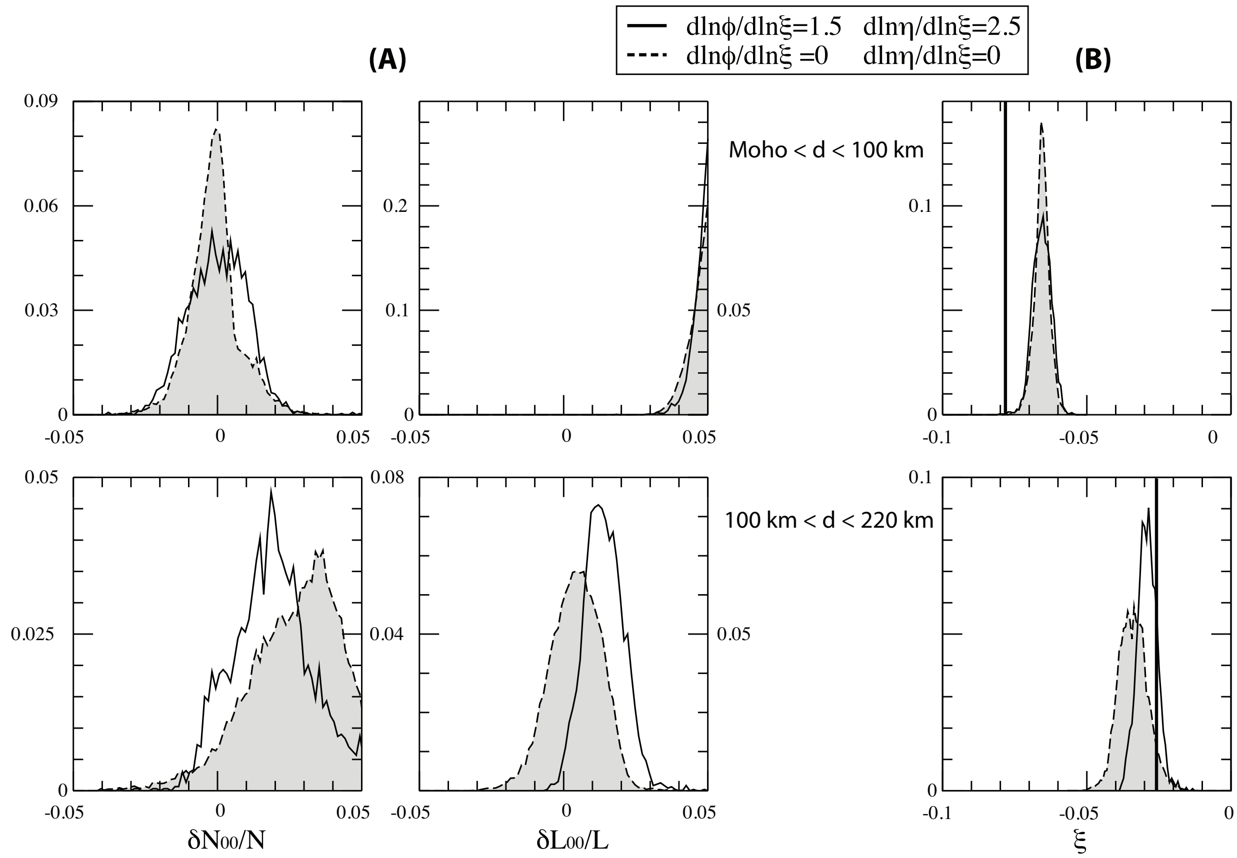

Figure 3. Comparison of posterior δN_s^t, δL_s^t, and ξ model distributions at spherical harmonic degree zero between a case where traditional prior scaling values are chosen (solid lines) and a case where perturbations in $d\eta$ and $d\phi$ are neglected (dashed lines). These distributions are not normalized. The vertical lines correspond to the value of ξ in PREM.

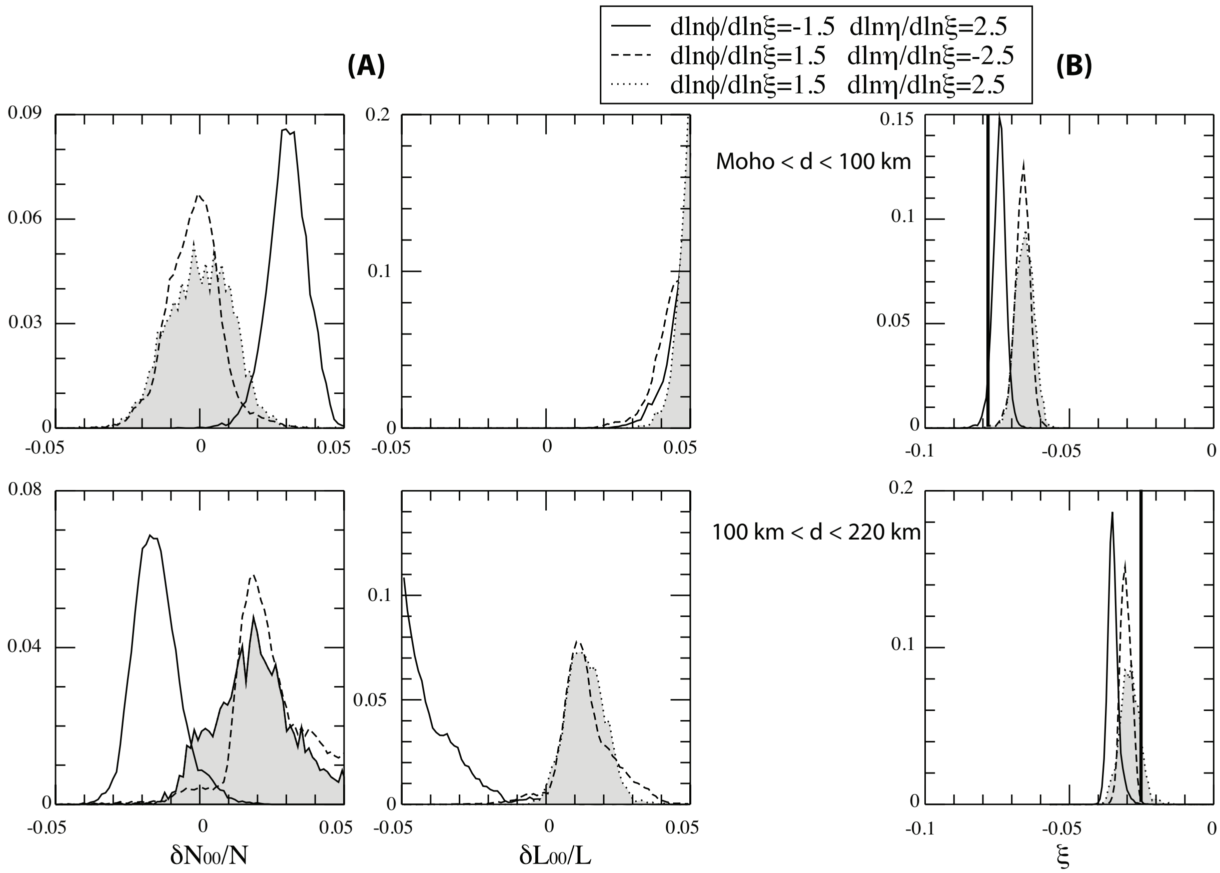

Figure 4. Comparison of posterior δN_s^t, δL_s^t distributions at spherical harmonic degree zero, and corresponding ξ distributions for different choices of prior scalings between anisotropic parameters. Dotted lines correspond to distributions obtained using traditional scaling values; Dashed lines correspond to distributions obtained by changing the sign of the ratio between P- and S-wave anisotropy; Solid lines were obtained by changing the sign of the ratio between η- and S-wave anisotropy. These distributions are not normalized. The vertical lines correspond to the value of ξ in PREM.

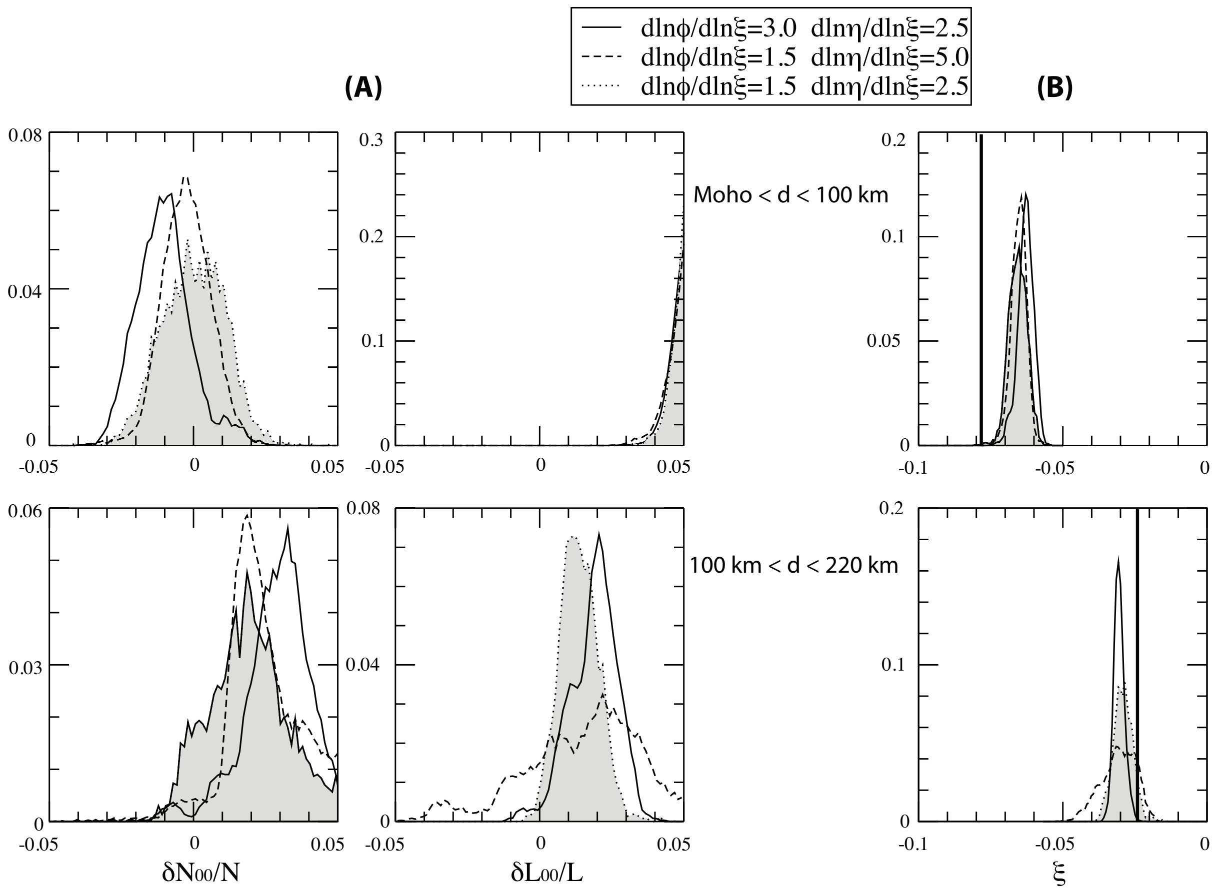

Figure 5. Comparison of posterior δN_s^t, δL_s^t distributions at spherical harmonic degree zero, and corresponding ξ distributions for different choices of prior scalings between anisotropic parameters. Dotted lines correspond to distributions obtained using traditional scaling values; Dashed lines correspond to distributions obtained by doubling the ratio between P- and S-wave anisotropy; Solid lines were obtained by doubling the ratio between η- and S-wave anisotropy. These distributions are not normalized. The vertical lines correspond to the value of ξ in PREM.

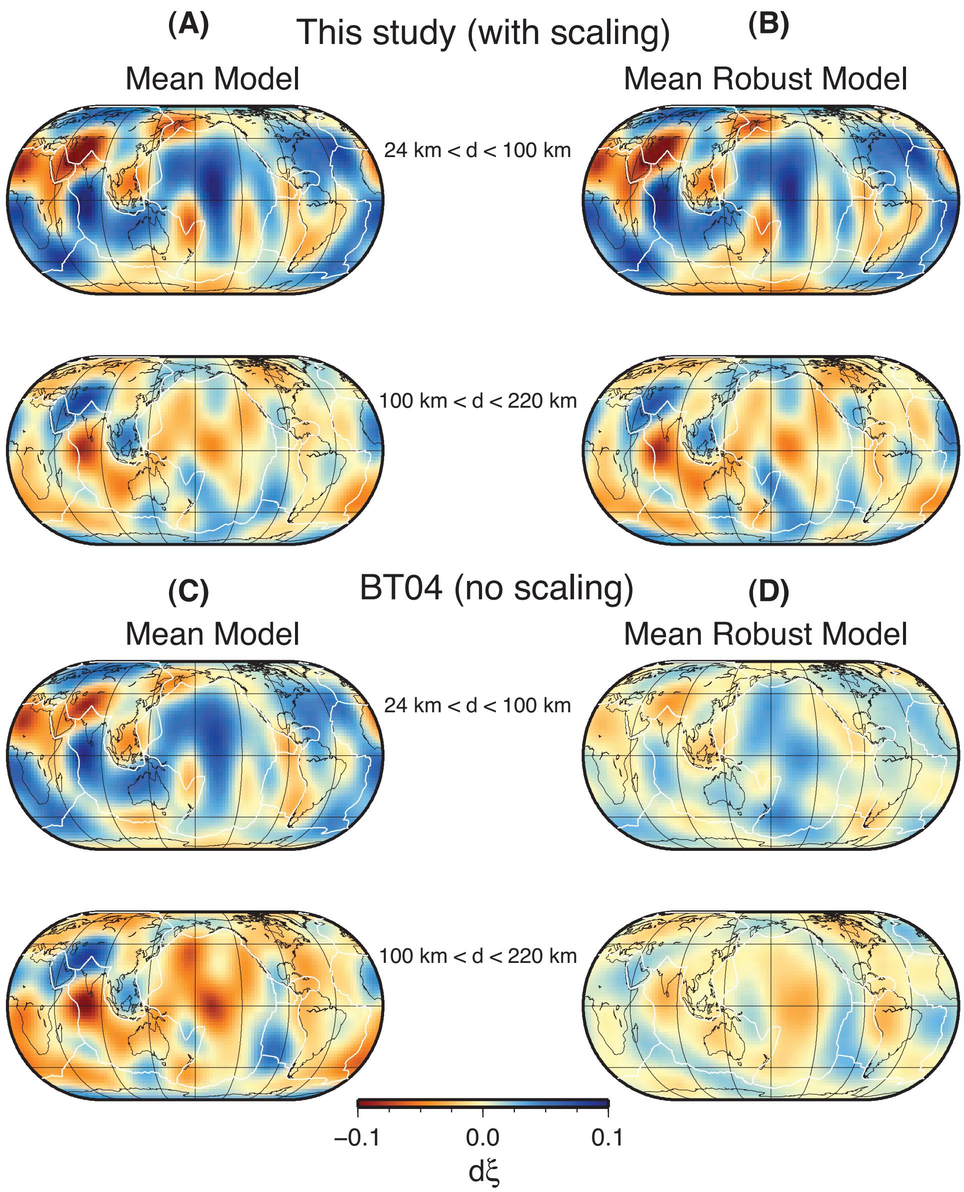

Figure 6. Perturbations in shear-wave anisotropy with respect to PREM. Panels (A) and (C) display the model obtained from the mean δL_s^t and δN_s^t values; Panels (B) and (D) display the "mean robust" model as defined in section 4. The upper four maps ((A) and (B)) correspond to models obtained in this study, with prior constraints on the elastic parameters, and the lower four maps ((C) and (D)) correspond to models from BT04 *Beghein and Trampert* [2004a] (without prior petrological constraints).

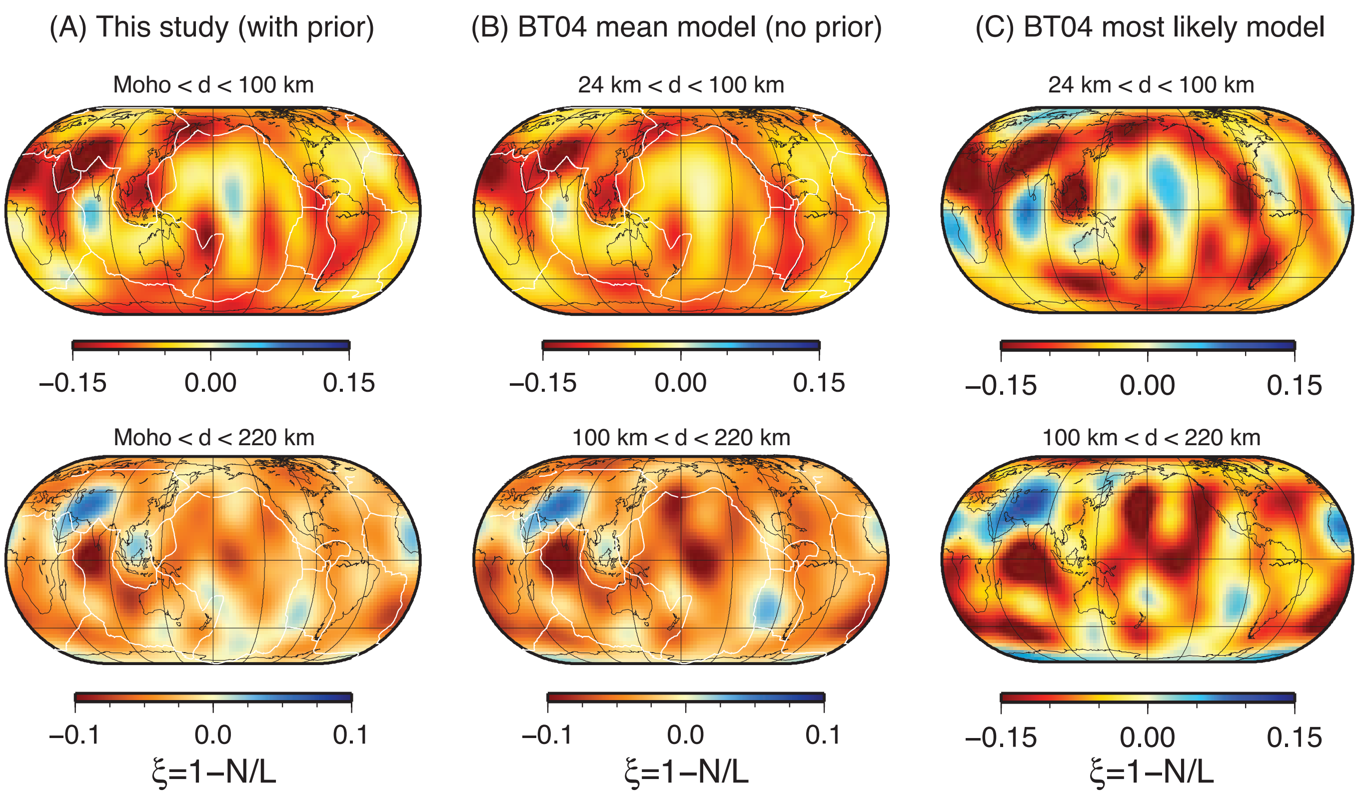

Figure 7. (A) Mean model for the absolute shear-wave radial anisotropy obtained with prior scaling relationships between anisotropic parameters; (B) Mean BT04 model obtained without prior information; (C) Most likely BT04 model.

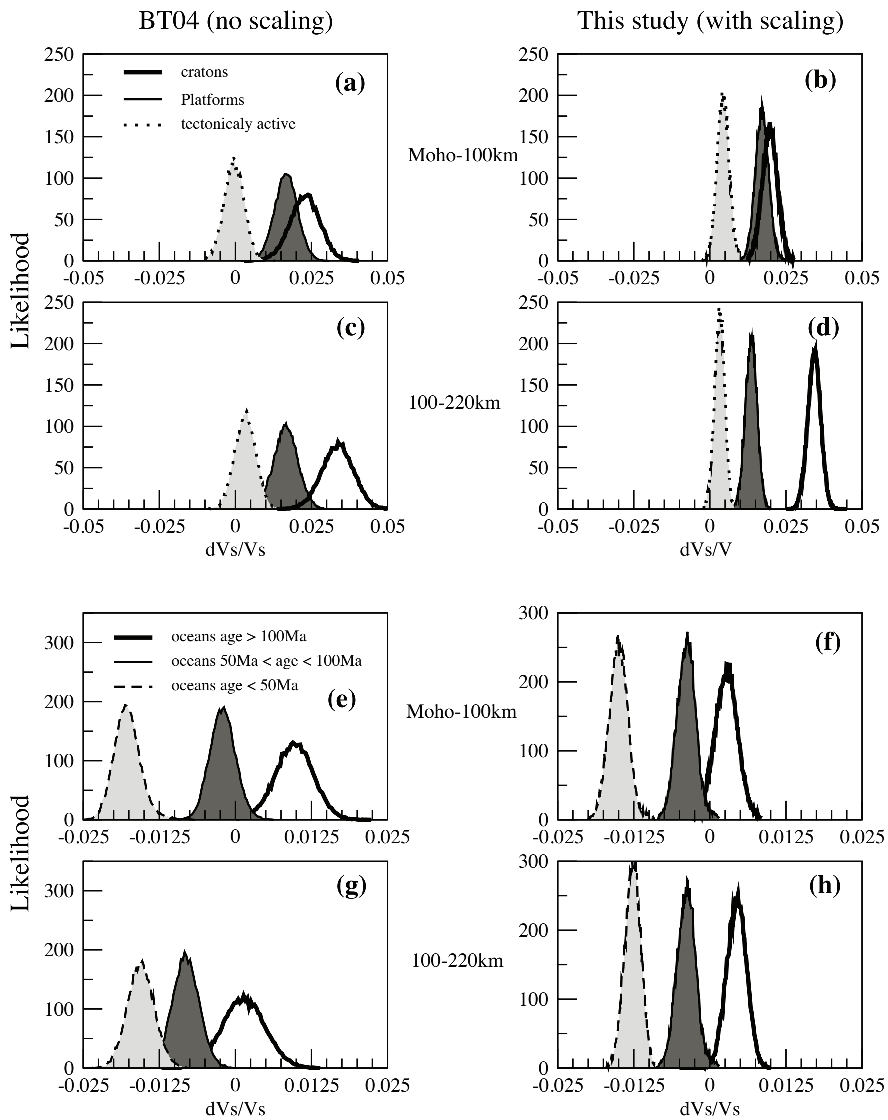

Figure 8. Likelihood of shear-wave velocity anomalies in various tectonic settings obtained without prior petrological constraints (left) and with prior constraints (right). (a)-(d) correspond to likelihoods for models averaged over all cratons, continental platforms or tectonically active areas. Panels (e)-(h) correspond to distribtuions of models averaged over oceanic regions sorted according to the age of the lithosphere

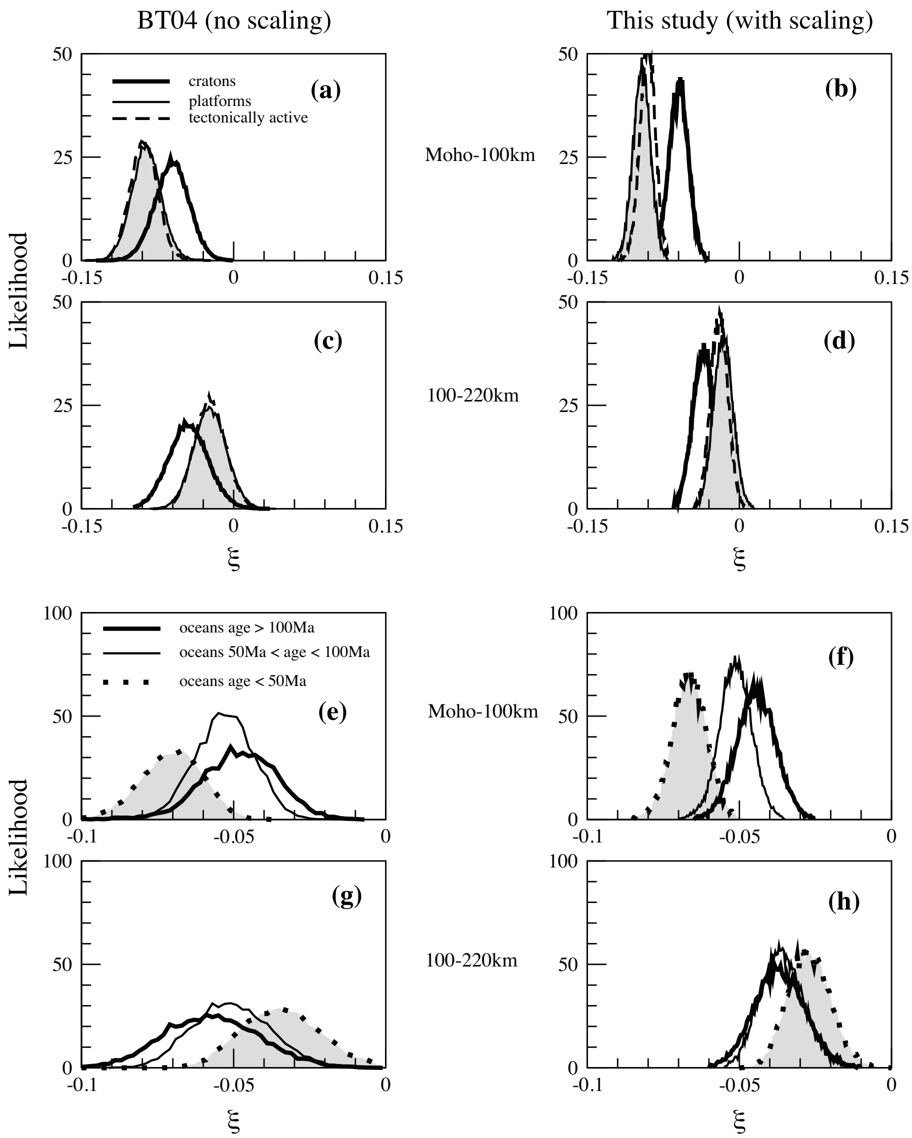

Figure 9. Likelihood of shear-wave radial anisotropy in various tectonic settings obtained without *a priori* constraints (left) and with *a priori* conformation (right). (a)-(d) correspond to likelihoods for models averaged over all cratons, continental platforms or tectonically active areas. Panels (e)-(h) correspond to distribtuions of models averaged over oceanic regions sorted according to the age of the lithosphere.